

Photo-sensitive 2D Arrangement of  $\text{-OH/H}_2\text{O}$  on Brookite  $\text{TiO}_2(210)$ 

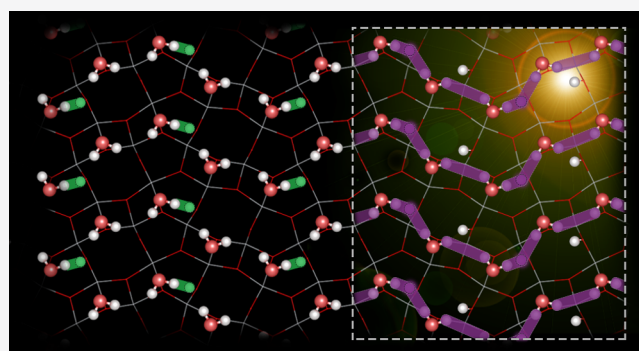
Lei Yang,\* Takumi Igarashi, Yu Cao, Eero Holmström, Kaito Hirata, Hitoshi Asakawa, Teruhisa Ohno, Takeshi Fukuma, and Adam S. Foster

 Cite This: *J. Phys. Chem. C* 2020, 124, 19091–19100 Read Online

ACCESS |

 Metrics & More Article Recommendations Supporting Information

**ABSTRACT:** The brookite phase of  $\text{TiO}_2$  is much less explored than the other two polymorphs, rutile and anatase, despite its potential applications in photo-catalytic  $\text{CO}_2$  reduction and water splitting. The first hydration layer and surface hydroxyl groups on the brookite (210) surface and their structural changes under photo-irradiation have been considered to play significant roles in such applications. Hence, in this work, we focus on studying them at the atomic scale using a combination of liquid-environment frequency modulation atomic force microscopy (FM-AFM) and density functional theory (DFT) calculations. The striped feature found in AFM images and its photo-switching behavior accompanied by photo-increased surface hydrophilicity are revealed by *ab initio* molecular dynamics simulations to originate from photo-sensitive two-dimensional arrangements of molecular and dissociative  $\text{H}_2\text{O}$  and proton-hopping behavior. The formation mechanism of the arrangements is further clarified by DFT static and nudged-elastic-band calculations.



## INTRODUCTION

$\text{TiO}_2$  has been well-known for decades because of its capability to decompose water into hydrogen and oxygen under irradiation, as discovered by Fujishima and Honda;<sup>1</sup> this remains at the core of photoelectrochemistry because of its high efficiency, nontoxicity, chemical and biological stabilities, and low cost.<sup>2</sup> Under ambient conditions, it is generally described to occur as three different polymorphs: rutile, anatase, and brookite.<sup>3</sup> While rutile and anatase have attracted considerable attention for various applications such as dye-sensitized solar cells, photocatalysis, pigments, and sensor devices,<sup>4–8</sup> the brookite phase remains the least studied mainly because of the difficulty in the preparation of its pure phase.<sup>2,9</sup> Recently, synthetic schemes to efficiently improve the purity of brookite  $\text{TiO}_2$  were devised,<sup>10–14</sup> bringing new interest in its potential applications.<sup>15–26</sup> In terms of catalytic activity, the brookite polymorphs were found to be good performers for photoelectrocatalytic  $\text{CO}_2$  reduction,<sup>15,16</sup>  $\text{H}_2$  evolution,<sup>17–20</sup> and organic degradation under ultraviolet irradiation.<sup>21–27</sup> The activity becomes even more profound in heterogeneous catalysis by mixing brookite with anatase or rutile and tuning their components for the heterogeneous system being studied.<sup>19,20,27</sup>

Among the brookite  $\text{TiO}_2$  surfaces, (210) draws the most attention because of its potential in (photo) electrocatalysis.<sup>28</sup> It covers as much as 33% of the exposed area of brookite  $\text{TiO}_2$  nanorods. With an atomic structure similar to the widely studied anatase  $\text{TiO}_2(101)$ , brookite (210) is capable of adsorbing and actively dissociating  $\text{H}_2\text{O}$  molecules as well.<sup>24,29</sup>

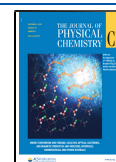
These two steps are elementary in the water splitting process on surfaces; in particular, the latter has been demonstrated to play a significant role.<sup>30</sup> However, the active sites on brookite (210) for water OH bond breaking are yet to be identified, and their catalytic mechanism is yet to be clarified. On the other hand, the structural change of the surface in the presence of water under photo-irradiation is also of great significance for photocatalytic applications.

The precise elucidation of how the active sites are arranged and how photo-irradiation would change the surface structure requires a technique with real atomic-scale resolution and access to the surface/interface. To this end, laboratory-developed liquid-environment ultralow noise frequency modulation atomic force microscopy (FM-AFM) is used in this study,<sup>31–33</sup> which features spatial resolution on a sub-nanometer length scale for imaging individual hydration layers.<sup>34,35</sup> However, it is still difficult to directly visualize structural changes that irradiation has induced at the surface because of the great challenge in the reconstruction of the real structures of the objective from the measured AFM images. *Ab initio* molecular dynamics (AIMD) simulation has been proven to provide a link between measured images and surface

Received: June 7, 2020

Revised: July 12, 2020

Published: July 13, 2020



topography because it has the inherent advantage to predict dynamics and processes of reactions from atomic models with excellent accuracy. As such, AIMD simulations are employed in the present study to interpret the AFM images. Apart from that, *ab initio* static calculations and nudged elastic band (NEB) calculations are also performed to clarify the origin of the features of the obtained FM-AFM images before and after the irradiation.

## METHODS

**Experimental Methods. Synthesis of Brookite  $\text{TiO}_2$  Nanorods.** Brookite  $\text{TiO}_2$  nanorods were prepared using titanium bis(ammonium lactate)dihydroxide (TALH) as a starting material.<sup>36</sup> Five milliliters of TALH aqueous precursor (50%) and an aqueous solution containing urea (7 M) were mixed, and then, deionized water was added to reach a final volume of 50  $\text{cm}^3$ . The resulting solution was transferred into a Teflon cup. The Teflon cup was sealed with a stainless-steel jacket and then heated at 230  $^\circ\text{C}$  for 48 h in an oven. The resulting powder was separated by centrifugation and washed with Milli-Q water until the ionic conductivity of the supernatant was  $<10 \mu\text{S cm}^{-1}$ . The particles were dried under reduced pressure at 60  $^\circ\text{C}$  for 12 h.

**AFM Sample Preparation.** The brookite nanocrystals were dissolved in a pH 2 HCl solution to a concentration of 2 mg/mL. This acidic condition gives a positive charge to the brookite particles and prevents their aggregation.<sup>37</sup> The solution was vortexed for 5 min and sonicated for 5 min by an ultrasonic homogenizer (UX-050, Mitsui Electric). Immediately after sonication, 100  $\mu\text{L}$  of the solution was deposited on a cleaved mica substrate (01877-MB, SPI Supplies) and left for 10 min for the adsorption of nanocrystals. The deposited solution was removed by spinning the substrate with a rotation speed of 1000 rpm for 10 s and 5000 rpm for 3 s. The sample was heated at 70  $^\circ\text{C}$  for 30 min by a vacuum oven. This process helps to enhance the adhesion of the nanoparticles to the mica surface by eliminating the water between them. For a sample to be imaged after photoirradiation, we irradiated a 300 nm ultraviolet (UV) light to the sample for 24 h by a light-emitting diode light source (M300L4, Thorlabs).

**FM-AFM, Transmission Electron Microscopy, and Contact Angle Measurements.** The AFM measurements were performed with a custom-built frequency modulation atomic force microscope with an ultralow-noise cantilever deflection (density  $< 10 \text{ fm}/\text{Hz}^{1/2}$ ) sensor.<sup>31–33</sup> The atomic force microscope was operated with a commercially available AFM controller (ARC2, Oxford Instruments) with some modifications in the software. The AFM measurements were performed at room temperature in a 0.1 M KCl aqueous solution. A commercially available silicon cantilever (PPP-NCHAuD, Nanoworld) with a nominal spring constant of 42 N/m and a resonance frequency of 150 kHz in liquid was used. The tip side of the cantilever was coated with Si (thickness: 30 nm) by a dc sputter coater (K575XD, Emitech) before each AFM measurement to improve the reproducibility of atomic-resolution AFM imaging in the liquid.<sup>38</sup> Transmission electron microscopy (TEM) was performed by Hitachi, H-9000NAR. The contact angles were measured by DM-301 (model number of the system, produced by Kyowa). We used a 2  $\mu\text{L}$  droplet of Milli-Q water for the measurements.

**Computational Methods. Density Functional Theory-Molecular Dynamics Simulations.** To reproduce the

structures observed by AFM imaging before and after UV irradiation, two systems were constructed as the initial structures for MD simulations (see Figure 1). Both consist

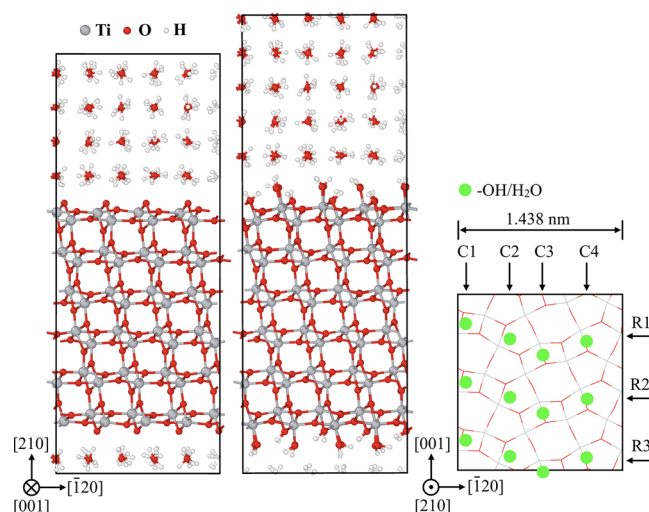


**Figure 1.** Side views of model ND (left) and model AD (middle) of the brookite  $\text{TiO}_2(210)/\text{H}_2\text{O}$  interface and the top view of the surface slab in model ND/AD (right). models ND and AD correspond to the cases before and after UV irradiation, respectively. C1–C4 indicate columns, and R1–R3 indicate rows. Green dots indicate positions of  $-\text{OH}/\text{H}_2\text{O}$  directly above the surface.

of a brookite  $\text{TiO}_2(210)$  surface slab and liquid water comprising 125  $\text{H}_2\text{O}$  molecules. In both models, the surface slabs were built by a previously reported approach<sup>29</sup> with lateral dimensions  $a = 3a_0$  and  $b = 2b_0$  ( $a/b/c$  axis corresponding to  $[001]/[120]/[210]$  direction), where  $a_0$  and  $b_0$  are the optimized lattice parameters of the bulk brookite  $\text{TiO}_2$  structure. The thickness of the slab in the  $c$  axis was determined to be 12 Ti layers by the convergence of the band gap at different thicknesses. An appropriate thickness of liquid water was adopted according to the fixed lateral lattice constants  $a$  and  $b$  to meet the experimental density of  $\text{H}_2\text{O}$  water 1.0  $\text{g}/\text{cm}^3$ . In MD simulations, the two centermost layers were frozen, and the lateral lattice constants  $a$  and  $b$  are fixed. The difference between the two models is that the surface of the former is clean, which allows  $\text{H}_2\text{O}$  molecules to spontaneously adsorb and naturally dissociate (ND) on it during the MD simulation, whereas the surface of the latter is fully covered by artificially dissociated (AD)  $\text{H}_2\text{O}$  molecules, that is, all outermost Ti atoms (denoted as  $\text{Ti}_{5\text{C}}$  because of it being 5-fold coordinated) are passivated with an  $-\text{OH}$  group and all outermost O atoms (denoted as  $\text{O}_{2\text{C}}$  because of it being 2-fold coordinated) are terminated with an  $\text{H}^+$  group. The latter model describing an extreme dissociation case with a 100% surface hydroxylation rate is inspired by the experimentally observed increase of surface hydrophilicity after irradiation (as presented in the section Results and Discussion). This shows that the consequently formed additional two  $-\text{OH}$  groups per  $\text{Ti}-\text{O}$  pair could provide more hydrogen bond donors and acceptors to  $\text{H}_2\text{O}$  molecules above them, thus making the surface more hydrophilic. This extreme case should not exist in reality, but by allowing the spontaneous recombination of  $-\text{OH}$  and  $\text{H}^+$  into  $\text{H}_2\text{O}$ , the system in the MD simulations is able to evolve to be closer to

reality. For convenience, these two models are denoted as model ND and model AD.

Density functional theory (DFT) MD calculations as implemented in CP2K<sup>39</sup> were performed within the generalized gradient approximation (GGA).<sup>40</sup> To appropriately evaluate the long-range dispersion interactions, which are important for accurately modeling of the solid–liquid interface and hydration layers, we employed Grimme D3 dispersion correction, which shows good agreement with the experimental results for several solid–liquid interfaces.<sup>41</sup> Goedecker–Teter–Hutter pseudopotentials<sup>42</sup> and a localized basis set of DZVP size<sup>43</sup> were chosen for all elements, with Ti 3s, 3p, 3d, and 4s and O 2s and 2p electrons explicitly treated. The surface slabs are optimized using 0.001 GPa and 0.05 eV/Å as the tolerance of stress and force, respectively. The Brillouin zone was sampled only at the  $\gamma$  point during the MD simulation, which is sufficient for large-size supercell structures. Using a Nose–Hoover chain thermostat with a time constant of 20 fs, constant temperature (NVT) conditions were maintained. The simulations were carried out at  $T = 400$  K, which is higher than room temperature, to accelerate dynamics on the one hand and, on the other hand, to yield good agreement with the experimental structural and diffusion properties of the liquid obtained at 298 K in GGA calculations at experimental water density.<sup>44–46</sup> The time step was set as 0.5 fs, which is justified to reproduce even the fastest dynamics in the system—OH stretching—by Born–Oppenheimer molecular dynamics. Each system was equilibrated for 12.5 ps, after which another 12.5 ps trajectory was collected for data analysis. Though the duration might not be sufficiently long for reproducing all the processes which would occur after the irradiation, in reality, it still provides insight into the trend of the structural evolution.

**DFT-Static and Kinetic Calculations.** The same DFT parameters were used to perform static calculations for configurations with different –OH/H<sub>2</sub>O arrangements. All the surfaces in these configurations are nearly the same as the one built for MD simulations, except being covered by one monolayer of H<sub>2</sub>O/–OH per surface Ti<sub>5C</sub> cation.

The transition barriers for H<sub>2</sub>O dissociation/reformation of single water molecules were evaluated at different positions on brookite (210) using the NEB method<sup>47,48</sup> with eight intermediate images and a force tolerance of 0.05 eV/Å. They are defined as

$$\Delta E_{\text{dissoc}}(E_{\text{reform}}) = E_{\text{TS}} - E_{\text{ini}}(E_{\text{fin}}) \quad (1)$$

where  $E_{\text{TS}}$ ,  $E_{\text{ini}}$ , and  $E_{\text{fin}}$  denote the total energy of the transition state, initial state (molecular H<sub>2</sub>O), and final state (dissociative H<sub>2</sub>O). The corresponding reaction time is estimated according to the Arrhenius equation<sup>49</sup> as

$$\tau = \frac{1}{A e^{-E_a/k_B T}} \quad (2)$$

where  $A$  (the pre-exponential factor) can be approximated as the H-bonded OH stretching frequency ( $10^{14}$  Hz),<sup>50</sup>  $k_B$  is the Boltzmann constant, and  $T = 298$  K.

## RESULTS AND DISCUSSION

**Experiments.** The TEM images of brookite TiO<sub>2</sub> (Figure 2a) confirmed a rod-shape structure with a smooth morphology, with most of the surface presenting {210} and {212} surfaces, as illustrated by Figure 2b. The lower-

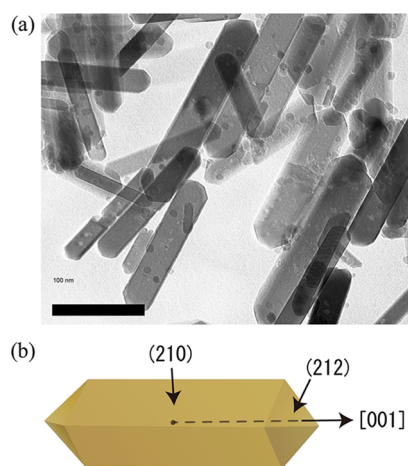


**Figure 2.** TEM image (a) and exposed crystal faces (b) of TiO<sub>2</sub> nanorods.

magnification AFM image of the (210) facet (Figure 3a) certified that an atomically flat terrace was obtained through the developed synthetic method. The close-up AFM image (Figure 3b) displays clear atomic-scale contrasts, confirming the capability of the custom-built FM-AFM to directly visualize atomic-scale surface features.

Significant differences between the AFM images taken before and after UV irradiation are observed from the comparison, as displayed in Figure 3b,c. Before the irradiation, it can be seen that there are four straight stripes (see the vertical arrows) within a unit cell's range (14.3 Å) along the [001] direction, consistent with the periodicity of the Ti<sub>5C</sub>/O<sub>2C</sub> atoms in the surface's atomistic model (see C1–C4 in Figure 1). Among these four stripes, one or two is regularly brighter than the others. A similar AFM feature was reported by Asakawa *et al.*,<sup>37</sup> however, its formation mechanism was not clarified. After the irradiation, in addition to the stripes along the [001] direction, those along  $[\bar{1}20]$  (see horizontal arrows) also arise. The contrast brightness of each particle becomes more moderate, leading to enhanced periodicity in the  $[\bar{1}20]$  direction and connection of the originally separated stripes.

In order to evaluate the hydrophilicity of the brookite TiO<sub>2</sub>(210) surface, water contact angle measurements were performed on a mica surface with TiO<sub>2</sub> nanoparticles deposited on it (Figure 3a). The angle is determined as 7.9° before irradiation, which becomes zero after the irradiation, indicating that the irradiation causes the hydrophilic surface to become superhydrophilic. Such photo-induced hydrophilicity has been reported in previous studies of anatase TiO<sub>2</sub><sup>51</sup> and other metal oxides.<sup>52</sup> The exact atomic structural change under photo-irradiation could not be visualized directly; hence, the origin of the photo-induced hydrophilicity has always been controversial. Some of these studies claimed that the increased hydrophilicity results from the photo-induced clean-up of organic surface contaminations.<sup>53–55</sup> However, there are also arguments suggesting that it is attributed to the increase of dissociative H<sub>2</sub>O molecules on the surface induced by photo-irradiation.<sup>47,48,56,57</sup> For the present study, the latter explanation makes more sense as we found no significant change in the amount of the surface contaminants on the nanorods before and after the UV irradiation. Aside from being the cause of the increased hydrophilicity, we believe the photo-induced additional dissociative H<sub>2</sub>O has a close relation with the

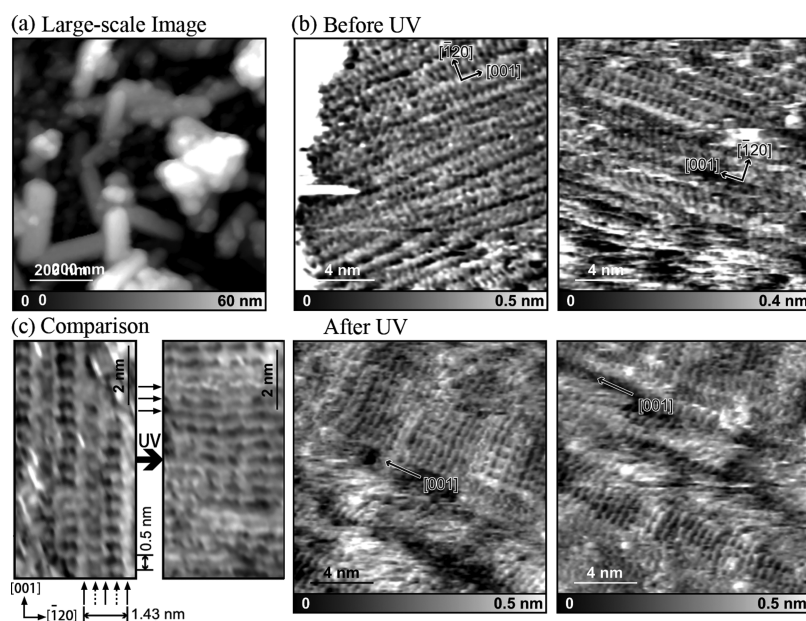


**Figure 3.** (a) Large-scale AFM images of  $\text{TiO}_2$  nanorods, (b) small-scale AFM images measured before and after UV irradiation, and (c) close-up comparison between the images measured before and after UV irradiation.

change in AFM patterns under irradiation as well. We will explore this hypothesis by the following DFT calculations.

**Simulations. DFT Dynamics.** Using model ND and AD as the initial structures, two MD simulations were performed to reproduce the dynamics before and after the irradiation, respectively. From the MD trajectories, the number densities of O as a function of distance  $z$  along the  $[210]$  direction from the outermost oxygens of the surface were derived (see Figure 4a). Each of the two profiles shows two distinct peaks, which correspond to the first and second hydration layers directly above the surface. The first peak for model AD is roughly at the same position with the same height as that for model ND. However, the second peak for model AD is notably higher than that for model ND. To clarify the reason, the radial distribution functions between the H of the  $-\text{OH}$  group in the first hydration layer and O in other water layers for model AD/ND were calculated and shown in Figure 4b. It is observed that the number of O within the first peak (1.40–2.35 Å) in model AD is 10% higher than that in model ND, indicating that in the former case, more  $\text{H}_2\text{O}$  in the second layer are “captured” through forming hydrogen bonds with the  $-\text{OH}$  fragment in the first layer. The higher capability to capture  $\text{H}_2\text{O}$  molecules also partly accounts for the higher hydrophilicity of the surface. Throughout the whole simulation, every  $\text{Ti}_{5\text{C}}$  is terminated with an O atom belonging to either an  $-\text{OH}$  group or an adsorbed  $\text{H}_2\text{O}$ , eliminating the possibility that the dark dots appearing in the AFM pattern are caused by a fragmentary hydration layer.

Because the brookite (210) surface exhibits the capability of dissociating  $\text{H}_2\text{O}$ , it is important to consider whether the stripes in the AFM pattern are related to this dissociation. To this end, the surface hydroxyl coverage—the percentage of surface  $\text{Ti}_{5\text{C}}$  cations passivated with an  $-\text{OH}$  fragment (e.g. 100% defined here as one  $-\text{OH}$  per  $\text{Ti}_{5\text{C}}$  cation)—as a function of simulation time was calculated, which is shown at the top of Figure 5. In the case of model ND, the closest  $\text{H}_2\text{O}$  molecules start to approach the surface as soon as MD begins. Within 1 ps, these molecules are adsorbed onto the surface,

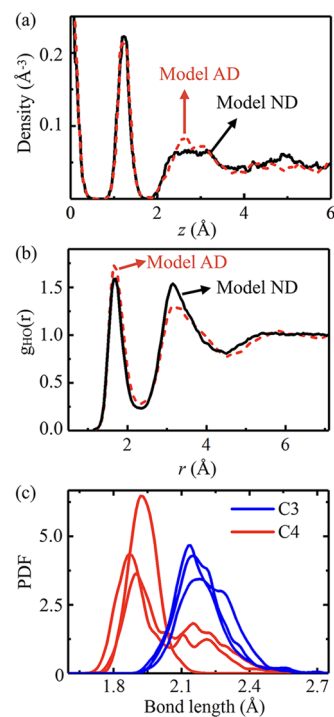


**Figure 4.** (a) Number densities of the O atom as a function of the distance  $z$  from the topmost O of the surfaces in models ND and AD; (b) radial distribution functions between the first-layer H and water O of models ND and AD (the first peak corresponding to  $\text{H}_{\text{L}1}\cdots\text{O}_{\text{L}2}$  hydrogen bonds); (c) probability density functions of bond lengths of  $\text{Ti}_{5\text{C}}-\text{O}_{\text{L}1}$  in C3 (blue) and C4 (red) of model ND. All data are derived from MD trajectories after equilibration.

and all clean  $\text{Ti}_{5\text{C}}$  atoms become  $-\text{H}_2\text{O}$  terminated. Because there is no  $\text{H}_2\text{O}$  dissociation at the beginning, the hydroxyl coverage starts from zero. As time progresses, the coverage increases gradually because of spontaneous  $\text{H}_2\text{O}$  dissociation and finally converges at  $\sim 30\%$ . In the case of the AD model, the coverage starts from 100% because all  $\text{Ti}_{5\text{C}}$  are artificially

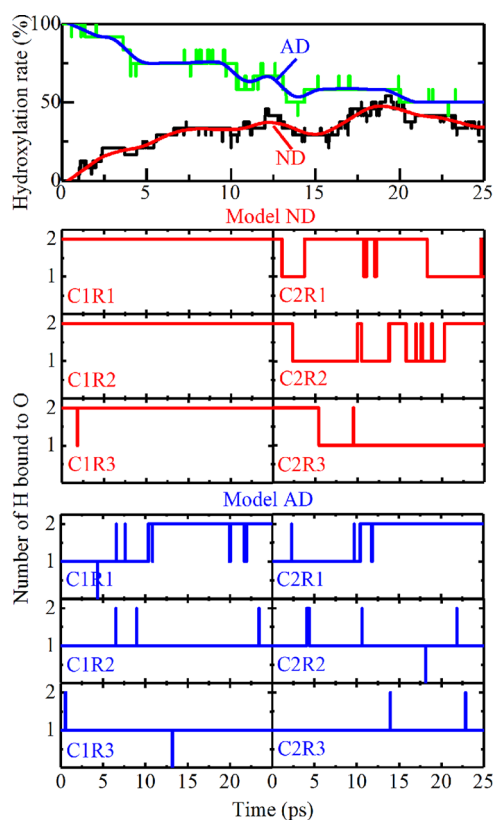


**Figure 5.** Time evolution of surface hydroxyl coverage (top) and numbers of H bound to the O of  $-\text{OH}/\text{H}_2\text{O}$  at different positions for models ND and AD (bottom). The positions are defined by columns C1–C4 and rows R1–R3 that are indicated in Figure 1. The rest columns are plotted in Figure S1.

terminated with  $-\text{OH}$  at the beginning. As time increases, the coverage drops gradually because of the combination of the  $-\text{OH}$  group on  $\text{Ti}_{5\text{C}}$  and  $\text{H}^+$  on  $\text{O}_{2\text{C}}$  forming an  $\text{H}_2\text{O}$  molecule. The coverage stabilizes at 50% after  $\sim 12$  ps, which is  $\sim 20\%$  higher than model ND, explaining the hydrophilicity

difference between the cases before and after irradiation observed in the water contact angle analysis. It might finally converge to the rate obtained from the simulation for model ND, but the difference between them would last for a relatively long time.

To understand how these  $-\text{OH}/\text{H}_2\text{O}$  groups are arranged on the surface and clarify whether they contribute to the one-dimensional feature observed in AFM images, we further decomposed the averaged surface hydroxyl coverage in terms of rows (R) in the  $[120]$  direction and columns (C) in the  $[001]$  direction (see the bottom of Figures 5 and S1); by this, we mean the number of H atoms bound to each of the 12 individual O atoms is in either surface  $-\text{OH}$  or  $\text{H}_2\text{O}$  in the supercell. In the case of model ND, it is observed that in C2 (identical to C4 because of the supercell's symmetry),  $\text{H}^+$  hops back and forth from  $\text{H}_2\text{O}$  to  $\text{O}_{2\text{C}}$  in the adjacent column, forming an  $-\text{OH}$  fragment or reforming an  $\text{H}_2\text{O}$  molecule. The statistics show that the adsorbed  $\text{H}_2\text{O}$  molecules are in a molecular form for 60% of the total data collecting period and dissociatively in the remaining 40%. Whereas in C1 (identical to C3), they remain intact almost throughout the whole period. Over an average of the four columns, the hydroxylation rate of the total surface was calculated to be  $\sim 30\%$ . It is worth noting that all molecular  $\text{H}_2\text{O}$  are arranged in straight lines, and all of those frequently switching between molecular and dissociative  $\text{H}_2\text{O}$  are arranged in other straight lines. These two species standing in different lines are periodically separated from each other and alternately parallel, arranged along the  $[120]$  direction with the regularity of one out of two columns, the periodicity of which is consistent with part of the AFM feature observed before the irradiation. To examine whether adsorbed  $-\text{OH}$  and  $\text{H}_2\text{O}$  can be distinguished structurally by AFM, regardless of the positions of H, the probability distribution of  $\text{Ti}_{5\text{C}}-\text{O}$  (either of  $-\text{OH}$  or  $-\text{H}_2\text{O}$ ) bond lengths in C3 and C4 was studied (see Figure 4c). It shows that the bond lengths in C4 can be assigned to two peaks, which center around 1.9 and 2.2 Å, corresponding to dissociative and molecular states, respectively, whereas the ones in C3 only contain one peak, at 2.2 Å. Hence, the  $\text{Ti}_{5\text{C}}-\text{O}$

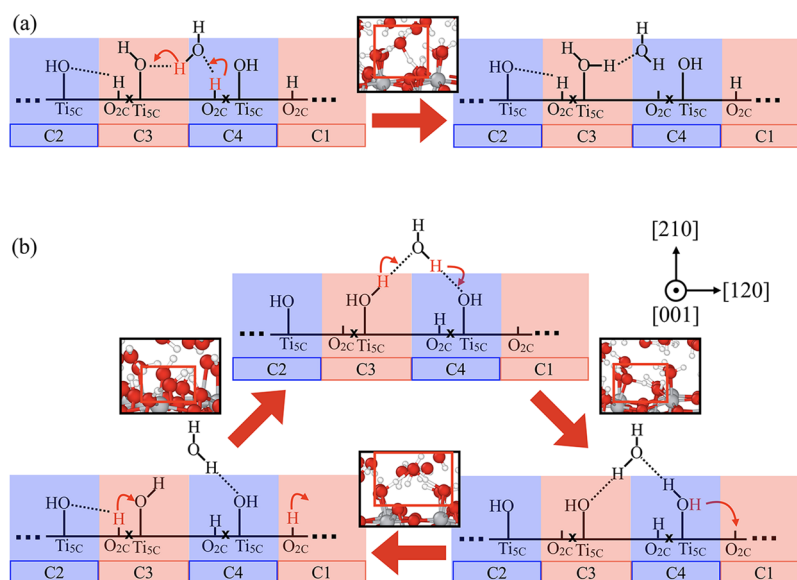


**Figure 6.** Schematic illustration of proton transfer processes between columns in model AD. “x” indicates that the actual distance between  $\text{Ti}_{5\text{C}}$  and  $\text{O}_{2\text{C}}$  in the same column is longer in a 3D space than in the 2D schematic. Insets show the snapshots of the transition states between structures.

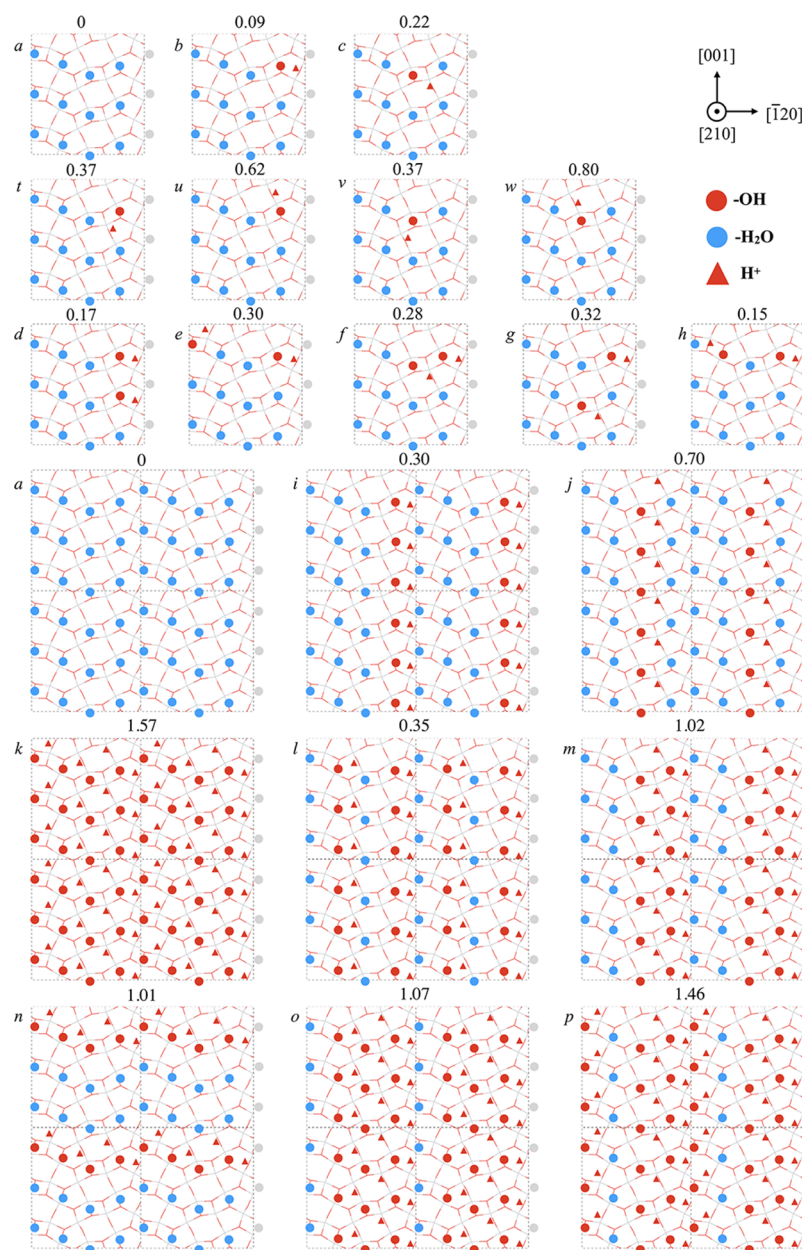


**Figure 7.** Configurations with different arrangements of  $-\text{OH}/\text{H}_2\text{O}$  and the corresponding energies. Grey and red indicate Ti and titanium O atoms, respectively. Conf *a*: fully water covered; conf *b* and *c*: with one water molecule dissociating in a certain column, where the  $\text{H}^+$  hops to  $\text{O}_{2\text{C}}$  in a different column; conf *t*–*w*: with one water molecule dissociating, where the  $\text{H}^+$  hops to  $\text{O}_{2\text{C}}$  in the same column; conf *d*–*h*: with two water molecules dissociating assuming the first taking place in C4; conf *i*, *j*: with a column of water dissociating; conf *l*, *m*: with two columns of water dissociating upon the water in C4 having dissociated; conf *o*, *p*: with three columns of water dissociating; conf *k*: with all (4 columns of) water dissociating; conf *n*: with one row of water dissociating.

bonds in C2/C4 are on average shorter than those in C1/C3, which might account for the difference in the AFM contrast between the columns. Nonetheless, it is not completely clear whether C2/C4 corresponds to brighter or darker stripes in the AFM image because AFM contrast is a complicated result of the interaction between the surface and tip and their hydration layers,<sup>58</sup> as yet no model for AFM imaging of OH groups in liquid has been developed.

In the case of model AD, it appears that the combination of  $-\text{OH}$  and  $\text{H}^+$  takes place randomly on the surface sites, regardless of which row or column they are located during the equilibration. It is observed that in some cases,  $\text{H}^+$  on  $\text{O}_{2\text{C}}$  at C2/C4 hops to the  $-\text{OH}$  at C1/C3 by the Grotthus

mechanism<sup>59,60</sup> through taking advantage of an  $\text{H}_2\text{O}$  molecule in the second hydration layer as a medium (see Figure 6a). Beyond that, some of the  $\text{H}^+$  on  $\text{O}_{2\text{C}}$  in C1/C3 combine with adjacent  $-\text{OH}$  in the same column to form a  $\text{H}_2\text{O}$  molecule (see lower left Figure 6b and conf *v* in Figure 7), which never occurs in the case of model ND because there is no  $-\text{OH}$  in C1/C3. These  $\text{H}^+$  can be further transferred to  $-\text{OH}$  at C2/C4 by the Grotthus mechanism and then to  $\text{O}_{2\text{C}}$  at C1/C3 to complete a cycle, as illustrated by Figure 6b. The proton hopping takes place so frequently between each adjacent two columns that all the protons belonging to  $-\text{OH}$  and  $\text{H}_2\text{O}$  are dynamic. On average, each  $\text{H}_2\text{O}$  stays in the molecular state for 50% of the time and in the dissociative state for the remaining

50%, accounting for the 50% hydroxylation rate of the total surface. The AFM tip oscillates much slower than the switching between these two states; thus, it should measure the interaction averaged over several oscillation cycles. In this sense, every  $-\text{OH}/\text{H}_2\text{O}$  site should have equal contrast. This illustrates a possible mechanism to explain why the AFM contrast brightness of each particle becomes more moderate after the irradiation and why the stripes become interconnected.

**DFT Statics and Kinetics.** To understand the preferred arrangements of  $-\text{H}_2\text{O}$  or  $-\text{OH}$  on the surface before the irradiation, DFT static calculations for 20 configurations of  $-\text{OH}/\text{H}_2\text{O}$  are performed (see Figure 7). From the ranking of their energies, we can infer that conf *a* is the most energetically favorable configuration, where all  $\text{Ti}_{5\text{C}}$  are passivated with molecularly adsorbed  $\text{H}_2\text{O}$ . Hence, the energy of conf *a* is set as zero, and energies of all other configurations are referenced to this. Because of the supercell's symmetry, the dissociation energies of  $\text{H}_2\text{O}$  at each of the three sites in different rows but the same column should be identical. Therefore, only one configuration for the dissociation in a certain column should be considered. The calculated total energy of conf *b*—the most stable configuration with one  $\text{H}_2\text{O}$  dissociation, where the dissociation takes place in C4 (identical to C2) and  $\text{H}^+$  hops to  $\text{O}_{2\text{C}}$  in C3/C1—is 0.09 eV. This is slightly higher than the case before dissociating, consistent with the value 0.05 eV reported in ref 28. The minor stability difference between this dissociated state and the molecular state explains why they have roughly the same occurrence probability 60 and 40%, although it might be slightly influenced by the absence of water layers in the static calculations. Conf *c* with dissociation in C3 (identical to C1)—another case where only one  $\text{H}_2\text{O}$  dissociates—turns out to be of much higher energy (0.22 eV). This calculated energy difference with respect to the molecular state is consistent with ref 28 (0.20 eV) as well.

The reason why conf *b* is more energetically favorable than conf *c* is suggested by the analysis of charge transfer during  $\text{H}_2\text{O}$  dissociation (see Table 1). We calculated the Hirshfeld

**Table 1.** Calculated Hirshfeld Charges of Atoms Ti1, OS1, Ti2, and OS2 Marked in Figure 8

	Ti1	OS1	Ti2	OS2
clean surface	0.07	-0.07	0.05	-0.04
conf <i>a</i>	-0.02	-0.15	-0.02	-0.12
conf <i>b</i>	-0.01	-0.15		
conf <i>c</i>			-0.03	-0.23

charge<sup>61</sup> of each atom of the clean surface and the configurations *a*, *b*, and *c*. It is found that after  $\text{H}_2\text{O}$  adsorption, all the most relevant atoms, marked as Ti1, Ti2, OS1, and OS2 in Figure 8, gain electrons from the adsorbed  $\text{H}_2\text{O}$  molecule. When one  $\text{H}_2\text{O}$  dissociates in C2/C4, the amount of charge on these atoms remains almost the same. Whereas in the case of C1/C3 dissociation, OS2 becomes 0.11  $e^-$  more negatively charged. The charge redistribution during the dissociation reaction results in the high energy of conf *c*.

The other cases with one  $\text{H}_2\text{O}$  molecule dissociation, confs *t*, *u*, *v*, and *w*, where  $\text{H}^+$  belonging to  $\text{H}_2\text{O}$  in C1/C3 or C2/C4 hops to an adjacent  $\text{O}_{2\text{C}}$  site located in the same column, are of even higher energy. Conversely, it indicates that these states will soon revert to the molecular state. This explains why in the MD simulations for model AD, the  $\text{H}^+$  in C1/C3 hops to a

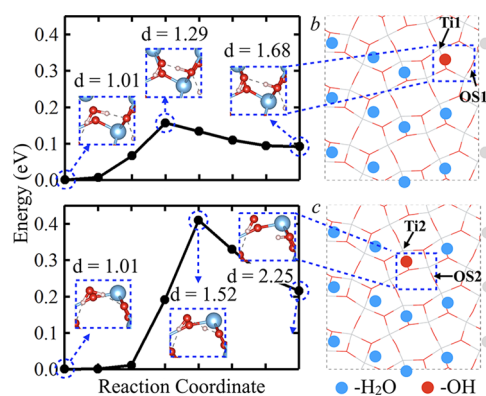


**Figure 8.** Potential energy surfaces of single  $\text{H}_2\text{O}$  dissociation in C4 (top) and C3 (bottom). “*d*” is the dissociation distance between O and H. The insets show the detailed atomic structures around the dissociative  $\text{H}_2\text{O}$ .

$-\text{OH}$  group in the same column to form  $\text{H}_2\text{O}$ . As mentioned before, this  $\text{H}^+$  could also hop to  $-\text{OH}$  in C2/C4—the choice of  $-\text{OH}$  depends on both the  $-\text{OH}$ 's orientation and its distance to this  $\text{H}^+$ .

Upon the first  $\text{H}_2\text{O}$  molecule dissociating at C4, the second dissociation will take place either in the same column (shown by conf *d*, 0.17 eV) or in C2 (shown by conf *h*, 0.15 eV) because their calculated energies are notably lower than the other cases, where the second dissociation takes place at C1 or C3 (conf *e*, *f*, and *g*: 0.30, 0.28, and 0.30 eV, respectively). Generally, it is believed that  $\text{H}^+$  generated by the second  $\text{H}_2\text{O}$  dissociation would experience repulsion from the adjacent  $\text{H}^+$  in the same column generated by the first dissociation, and in that sense, a zig-zag arrangement of them—the first  $\text{H}^+$  in C2 and the second one in C1/C3—would reduce the repulsion energy. However, the above result implies that it could not yet offset the high energy caused by the dissociation of  $\text{H}_2\text{O}$  in the unfavorable column C1/C3. Actually, the repulsive energy contribution is negligible, as shown by the fact that the energy of conf *d* referenced to molecular  $\text{H}_2\text{O}$  is approximately twice that of conf *b*. Nonetheless, the energy of the system is still somehow reduced when the two dissociations are arranged in two different columns C2 and C4, as illustrated by conf *h*. From the above analysis, we can assert that  $\text{H}_2\text{O}$  molecules prefer to dissociate in C2 or C4, regardless of coverage rate, as the structures formed in this way are more energetically favorable.

As the number of dissociated  $\text{H}_2\text{O}$  further increases, a huge number of configurations are to be considered. On this front, we only chose the cases where all the  $\text{H}_2\text{O}$  in certain columns dissociate for the sake of simplicity. This is also due to the fact that at this stage, we are more concerned with how many columns of  $\text{H}_2\text{O}$  could dissociate at ambient temperature, rather than how many  $\text{H}_2\text{O}$  could dissociate in certain columns. As shown in the MD simulations, these cases are unlikely to occur, though they still provide insight into the overall process. As shown in Figure 7, not surprisingly, the energy of conf *i* with all the dissociations taking place at C2 (0.30 eV, identical to C4) is lower than conf *j* where they take place in C1 (identical to C3). Assuming that all  $\text{H}_2\text{O}$  in C2 are already dissociated (corresponding to a 25% hydroxylation rate), we investigated where the second column of dissociated  $\text{H}_2\text{O}$  should locate (corresponding to a 50% hydroxylation rate). It appears that conf *l* with dissociations taking place at

C2 and C4 is more energetically favorable (0.35 eV) than conf *m* with C2 and C3 (or C1) dissociation. It is worth noting that the lowest energies of 1-column and 2-column dissociations are comparable (0.30 and 0.35 eV, respectively), indicating similar probabilities of their occurrence. The energy fluctuations resulting from the temperature could easily give rise to one or two incomplete columns of water dissociation, accounting for the one or two out of four column brightness regularly observed in AFM images. We also studied the cases where there are three columns or four columns (conf *o* and *p* or conf *k*, corresponding to 75 or 100% hydroxylation rate) of H<sub>2</sub>O dissociating—they are of so high energy that these cases are quite unlikely to occur. Another configuration (conf *n*) is designed to determine whether the dissociated H<sub>2</sub>O would stand in a row along the [120] direction, but this is also unfavorable.

The static calculations focused on the energy difference between the initial and final states during an H<sub>2</sub>O dissociation/reformation reaction. However, the reaction process itself is dependent on the energy barrier. To this end, the transition barrier for the dissociation and its inverse reaction (reformation of single water molecules) was evaluated at different positions. As shown in Figure 8, the calculated barrier of the dissociation at C2 (identical to C4) is 0.16 eV, corresponding to a mean reaction time of 5 ps at room temperature according to eq 2.<sup>62,63</sup> This process could be possibly accelerated in the presence of dynamic liquid water directly above the first hydration layer through lowering of the barrier, whereas the barrier for dissociation at C1 (identical to C3) is 0.41 eV. This much higher barrier with respect to that at C2 is partly caused by the greater distance that the proton needs to move during the reaction, as illustrated by the O⋯H dissociation distance “*d*” in Figure 8. The derived reaction time is beyond a scale reachable by DFT-MD simulations, but the reaction is still possible in rare cases at a longer time range at room temperature. However, the dissociated H<sub>2</sub>O will soon revert to the molecular state because of the notable energy difference between the two states.

Figure 8 also shows the energy barrier of the reaction where –OH and H<sup>+</sup> combined to form an H<sub>2</sub>O molecule. For the combination in C2 or C4, it is determined to be 0.08 eV, which is so small that H<sup>+</sup> can quickly hop back to reform –H<sub>2</sub>O, as observed in the MD simulation for model ND. For recombination in C1 or C3 the barrier is 0.22 eV, which is higher because of the long travel distance of H<sup>+</sup>. Hopping through the Grotthuss mechanism could shorten the distance and thus lower the barrier. Under the Grotthuss mechanism, H<sup>+</sup> hops to a H<sub>2</sub>O molecule acting as the medium in the first step, forming H<sub>3</sub>O<sup>+</sup> as the intermediate structure. In the second step, another H<sup>+</sup> of H<sub>3</sub>O<sup>+</sup> hops further to the target –OH through the hydrogen bond, as illustrated in Figure 6a. The shorter O⋯O distance (~2.6 Å) in each step indicates a shorter travel distance of the proton (~0.8 Å) compared to the original single-step reaction (O⋯O distance: ~3.1 Å, travel distance of the proton: ~1.3 Å). Because the energy barrier for proton transfer decreases as the O⋯O distance decreases,<sup>64,65</sup> the two-step reaction breaks the original high energy barrier into two lower ones.

## CONCLUSIONS

In summary, we have studied the hydration layers on the brookite (210) surface and their structural changes under photo-irradiation by liquid-environment FM-AFM and DFT

calculations. An interesting feature is shown in AFM images, in which the brighter contrast columns and the darker ones alternate along the [120] direction with the regularity of one in either two or four columns. After the surface is treated with photo-irradiation, it appears that the regularity in the [120] direction is also enhanced and the periodically separated stripes became interconnected; meanwhile, the surface becomes superhydrophilic. Based on the experimental result, we propose a hypothesis that these two changes result from photo-increased hydroxyl groups, according to which two initial models of *ab initio* MD simulations for the cases before and after the irradiation are designed. The MD simulations show that adsorbed H<sub>2</sub>O molecules prefer to dissociate in certain columns of Ti<sub>5C</sub> sites and remain in a molecular form in other columns. This may account for the brighter and darker stripes, respectively, observed in AFM images before irradiation. After irradiation, photo-induced additional hydroxyl groups cause the surface to be more hydrophilic, and frequent proton transfer between columns leads all the –OH/H<sub>2</sub>O units to have identical AFM contrast brightness. DFT static and kinetic modeling suggests why the dissociation/reformation of H<sub>2</sub>O only takes place in specific columns. While several questions still remain because of the limited timescale accessible to AIMD, the result of the study provides insight into the possible mechanisms of photo-induced surface hydrophilicity and contributes to understanding brookite’s water splitting activity.

## ASSOCIATED CONTENT

### Supporting Information

The Supporting Information is available free of charge at <https://pubs.acs.org/doi/10.1021/acs.jpcc.0c05151>.

Numbers of H bound to the O of –OH/H<sub>2</sub>O in columns other than those plotted in Figure 5 (PDF)

## AUTHOR INFORMATION

### Corresponding Author

Lei Yang – Nano Life Science Institute (WPI-NanoLSI), Kanazawa University, Kanazawa 920-1192, Japan; COMP Centre of Excellence, Department of Applied Physics, Aalto University, Helsinki FI-00076, Finland; Max-Planck-Institut für Eisenforschung GmbH, Düsseldorf 40237, Germany; [orcid.org/0000-0001-6357-2768](https://orcid.org/0000-0001-6357-2768); Email: [l.yang@staff.kanazawa-u.ac.jp](mailto:l.yang@staff.kanazawa-u.ac.jp)

### Authors

Takumi Igarashi – Division of Electrical Engineering and Computer Science, Kanazawa University, Kanazawa 920-1192, Japan

Yu Cao – Applied Chemistry Section, Department of Materials Science, Faculty of Engineering, Kyushu Institute of Technology, Kitakyushu, Fukuoka 840-8550, Japan

Eero Holmström – COMP Centre of Excellence, Department of Applied Physics, Aalto University, Helsinki FI-00076, Finland; [orcid.org/0000-0002-4866-3730](https://orcid.org/0000-0002-4866-3730)

Kaito Hirata – Division of Electrical Engineering and Computer Science, Kanazawa University, Kanazawa 920-1192, Japan

Hitoshi Asakawa – Division of Electrical Engineering and Computer Science and Nanomaterials Research Institute (NanoMaRi), Kanazawa University, Kanazawa 920-1192, Japan; [orcid.org/0000-0002-2320-2655](https://orcid.org/0000-0002-2320-2655)

**Teruhisa Ohno** – Applied Chemistry Section, Department of Materials Science, Faculty of Engineering, Kyushu Institute of Technology, Kitakyushu, Fukuoka 840-8550, Japan

**Takeshi Fukuma** – Nano Life Science Institute (WPI-NanoLSI) and Division of Electrical Engineering and Computer Science, Kanazawa University, Kanazawa 920-1192, Japan; [orcid.org/0000-0001-8971-6002](https://orcid.org/0000-0001-8971-6002)

**Adam S. Foster** – COMP Centre of Excellence, Department of Applied Physics, Aalto University, Helsinki FI-00076, Finland; Nano Life Science Institute (WPI-NanoLSI), Kanazawa University, Kanazawa 920-1192, Japan; [orcid.org/0000-0001-5371-5905](https://orcid.org/0000-0001-5371-5905)

Complete contact information is available at: <https://pubs.acs.org/10.1021/acs.jpcc.0c05151>

## Notes

The authors declare no competing financial interest.

## ACKNOWLEDGMENTS

The work has been performed under the project HPC-EUROPA3 (INFRAIA-2016-1-730897), with the support of the EC Research Innovation Action under the H2020 Programme. L.Y. and A.S.F. acknowledge the use of the computational resources provided by the Aalto Science-IT project and CSC, Helsinki. The work was also supported in part by the RIKEN Center for Computational Science through the HPCI System Research project hp200002. L.Y. acknowledges Tong Liu for support on TOC graphic and cover art. L.Y. was supported by the Strategic Research Promotion Program (Core-to-Core Program) and the Startup Fund Allocation for Assistant Professor of Kanazawa University. A.S.F. was supported by the Academy of Finland (project no. 314862). Y.C. and T.O. acknowledge the ENEOS Hydrogen Trust Fund. This work was also supported by the World Premier International Research Center Initiative (WPI), MEXT, Japan; JSPS KAKENHI (no. 16H02111); and the JST ACT-C project.

## REFERENCES

- (1) Fujishima, A.; Honda, K. Electrochemical Photolysis of Water at a Semiconductor Electrode. *Nature* **1972**, *238*, 37–38.
- (2) Di Paola, A.; Bellardita, M.; Palmisano, L. Brookite, the Least Known TiO<sub>2</sub> Photocatalyst. *Catalysts* **2013**, *3*, 36–73.
- (3) Zhu, T.; Gao, S.-P. The Stability, Electronic Structure, and Optical Property of TiO<sub>2</sub> Polymorphs. *J. Phys. Chem. C* **2014**, *118*, 11385–11396.
- (4) Inoue, T.; Fujishima, A.; Konishi, S.; Honda, K. Photo-Electrocatalytic Reduction of Carbon Dioxide in Aqueous Suspensions of Semiconductor Powders. *Nature* **1979**, *277*, 637–638.
- (5) Diebold, U. The Surface Science of Titanium Dioxide. *Surf. Sci. Rep.* **2003**, *48*, 53–229.
- (6) Wang, Y.; Li, J.; Wang, L.; Xue, T.; Qi, T. Preparation of Rutile Titanium Dioxide White Pigment via Doping and Calcination of Metatitanic Acid Obtained by the NaOH Molten Salt Method. *Ind. Eng. Chem. Res.* **2010**, *49*, 7693–7696.
- (7) Catlow, C. R. A.; Guo, Z. X.; Miskufova, M.; Shevlin, S. A.; Smith, A. G. H.; Sokol, A. A.; Walsh, A.; Wilson, D. J.; Woodley, S. M. Advances in Computational Studies of Energy Materials. *Philos. Trans. R. Soc., A* **2010**, *368*, 3379–3456.
- (8) Gupta, S. M.; Tripathi, M. A Review of TiO<sub>2</sub> Nanoparticles. *Chin. Sci. Bull.* **2011**, *56*, 1639–1657.
- (9) Penn, R. L.; Banfield, J. F. Oriented Attachment and Growth, Twinning, Polytypism, and Formation of Metastable Phases: Insights from Nanocrystalline TiO<sub>2</sub>. *Am. Mineral.* **1998**, *83*, 1077–1082.

(10) Tomita, K.; Petrykin, V.; Kobayashi, M.; Shiro, M.; Yoshimura, M.; Kakihana, M. A Water-Soluble Titanium Complex for the Selective Synthesis of Nanocrystalline Brookite, Rutile, and Anatase by a Hydrothermal Method. *Angew. Chem., Int. Ed.* **2006**, *45*, 2378–2381.

(11) Addamo, M.; Bellardita, M.; Di Paola, A.; Palmisano, L. Preparation and Photoactivity of Nanostructured Anatase, Rutile and Brookite TiO<sub>2</sub> Thin Films. *Chem. Commun.* **2006**, 4943–4945.

(12) Di Paola, A.; Addamo, M.; Bellardita, M.; Cazzanelli, E.; Palmisano, L. Preparation of Photocatalytic Brookite Thin Films. *Thin Solid Films* **2007**, *515*, 3527–3529.

(13) Cassaignon, S.; Koelsch, M.; Jolivet, J.-P. Selective Synthesis of Brookite, Anatase and Rutile Nanoparticles: Thermolysis of TiCl<sub>4</sub> in Aqueous Nitric Acid. *J. Mater. Sci.* **2007**, *42*, 6689–6695.

(14) Hu, W.; Li, L.; Li, G.; Tang, C.; Sun, L. High-Quality Brookite TiO<sub>2</sub> Flowers: Synthesis, Characterization, and Dielectric Performance. *Cryst. Growth Des.* **2009**, *9*, 3676–3682.

(15) Liu, L.; Zhao, H.; Andino, J. M.; Li, Y. Photocatalytic CO<sub>2</sub> Reduction with H<sub>2</sub>O on TiO<sub>2</sub> Nanocrystals: Comparison of Anatase, Rutile, and Brookite Polymorphs and Exploration of Surface Chemistry. *ACS Catal.* **2012**, *2*, 1817–1828.

(16) Kominami, H.; Ishii, Y.; Kohno, M.; Konishi, S.; Kera, Y.; Ohtani, B. Nanocrystalline Brookite-Type Titanium(IV) Oxide Photocatalysts Prepared by a Solvothermal Method: Correlation between Their Physical Properties and Photocatalytic Activities. *Catal. Lett.* **2003**, *91*, 41–47.

(17) Kominami, H.; Kato, J.-i.; Murakami, S.-y.; Ishii, Y.; Kohno, M.; Yabutani, K.-i.; Yamamoto, T.; Kera, Y.; Inoue, M.; Inui, T.; et al. Solvothermal Syntheses of Semiconductor Photocatalysts of Ultra-High Activities. *Catal. Today* **2003**, *84*, 181–189.

(18) Chiarello, G. L.; Di Paola, A.; Palmisano, L.; Selli, E. Effect of Titanium Dioxide Crystalline Structure on the Photocatalytic Production of Hydrogen. *Photochem. Photobiol. Sci.* **2011**, *10*, 355–360.

(19) Kandiel, T. A.; Feldhoff, A.; Robben, L.; Dillert, R.; Bahnemann, D. W. Tailored Titanium Dioxide Nanomaterials: Anatase Nanoparticles and Brookite Nanorods as Highly Active Photocatalysts. *Chem. Mater.* **2010**, *22*, 2050–2060.

(20) Ismail, A. A.; Kandiel, T. A.; Bahnemann, D. W. Novel (and Better?) Titania-Based Photocatalysts: Brookite Nanorods and Mesoporous Structures. *J. Photochem. Photobiol., A* **2010**, *216*, 183–193.

(21) Reddy, M. A.; Kishore, M. S.; Pralong, V.; Varadaraju, U. V.; Raveau, B. Lithium Intercalation into Nanocrystalline Brookite TiO<sub>2</sub>. *Electrochem. Solid-State Lett.* **2007**, *10*, A29–A31.

(22) Li, J.-G.; Ishigaki, T.; Sun, X. Anatase, Brookite, and Rutile Nanocrystals via Redox Reactions under Mild Hydrothermal Conditions: Phase-Selective Synthesis and Physicochemical Properties. *J. Phys. Chem. C* **2007**, *111*, 4969–4976.

(23) Iskandar, F.; Nandiyanto, A. B. D.; Yun, K. M.; Hogan, C. J.; Okuyama, K.; Biswas, P. Enhanced Photocatalytic Performance of Brookite TiO<sub>2</sub> Macroporous Particles Prepared by Spray Drying with Colloidal Templating. *Adv. Mater.* **2007**, *19*, 1408–1412.

(24) Ardizzone, S.; Bianchi, C. L.; Cappelletti, G.; Gialanella, S.; Pirola, C.; Ragaini, V. Tailored Anatase/Brookite Nanocrystalline TiO<sub>2</sub>. The Optimal Particle Features for Liquid- and Gas-Phase Photocatalytic Reactions. *J. Phys. Chem. C* **2007**, *111*, 13222–13231.

(25) Addamo, M.; Augugliaro, V.; Bellardita, M.; Di Paola, A.; Loddo, V.; Palmisano, G.; Palmisano, L.; Yurdakal, S. Environmentally Friendly Photocatalytic Oxidation of Aromatic Alcohol to Aldehyde in Aqueous Suspension of Brookite TiO<sub>2</sub>. *Catal. Lett.* **2008**, *126*, 58–62.

(26) Augugliaro, V.; Loddo, V.; López-Muñoz, M. J.; Márquez-Álvarez, C.; Palmisano, G.; Palmisano, L.; Yurdakal, S. Home-Prepared Anatase, Rutile, and Brookite TiO<sub>2</sub> for Selective Photocatalytic Oxidation of 4-Methoxybenzyl Alcohol in Water: Reactivity and ATR-FTIR Study. *Photochem. Photobiol. Sci.* **2009**, *8*, 663–669.

(27) Palmisano, L.; Augugliaro, V.; Bellardita, M.; Di Paola, A.; García López, E.; Loddo, V.; Marci, G.; Palmisano, G.; Yurdakal, S.

Titania Photocatalysts for Selective Oxidations in Water. *ChemSusChem* **2011**, *4*, 1431–1438.

(28) Li, W.-K.; Gong, X.-Q.; Lu, G.; Selloni, A. Different Reactivities of TiO<sub>2</sub> Polymorphs: Comparative DFT Calculations of Water and Formic Acid Adsorption at Anatase and Brookite TiO<sub>2</sub> Surfaces. *J. Phys. Chem. C* **2008**, *112*, 6594–6596.

(29) Holmström, E.; Ghan, S.; Asakawa, H.; Fujita, Y.; Fukuma, T.; Kamimura, S.; Ohno, T.; Foster, A. S. Hydration Structure of Brookite TiO<sub>2</sub> (210). *J. Phys. Chem. C* **2017**, *121*, 20790–20801.

(30) Zhao, W.-N.; Liu, Z.-P. Mechanism and Active Site of Photocatalytic Water Splitting on Titania in Aqueous Surroundings. *Chem. Sci.* **2014**, *5*, 2256–2264.

(31) Fukuma, T.; Kimura, M.; Kobayashi, K.; Matsushige, K.; Yamada, H. Development of Low Noise Cantilever Deflection Sensor for Multienvironment Frequency-Modulation Atomic Force Microscopy. *Rev. Sci. Instrum.* **2005**, *76*, 053704.

(32) Fukuma, T.; Jarvis, S. P. Development of Liquid Environment Frequency Modulation Atomic Force Microscope with Low Noise Deflection Sensor for Cantilevers of Various Dimensions. *Rev. Sci. Instrum.* **2006**, *77*, 043701.

(33) Fukuma, T. Wideband Low-Noise Optical Beam Deflection Sensor with Photothermal Excitation for Liquid-Environment Atomic Force Microscopy. *Rev. Sci. Instrum.* **2009**, *80*, 023707.

(34) Fukuma, T.; Ueda, Y.; Yoshioka, S.; Asakawa, H. Atomic-Scale Distribution of Water Molecules at the Mica-Water Interface Visualized by Three-Dimensional Scanning Force Microscopy. *Phys. Rev. Lett.* **2010**, *104*, 016101.

(35) Fukuma, T.; Garcia, R. Atomic- and Molecular-Resolution Mapping of Solid-Liquid Interfaces by 3D Atomic Force Microscopy. *ACS Nano* **2018**, *12*, 11785–11797.

(36) Kandiel, T. A.; Feldhoff, A.; Robben, L.; Dillert, R.; Bahnemann, D. W. Tailored Titanium Dioxide Nanomaterials: Anatase Nanoparticles and Brookite Nanorods as Highly Active Photocatalysts. *Chem. Mater.* **2010**, *22*, 2050–2060.

(37) Asakawa, H.; Holmström, E.; Foster, A. S.; Kamimura, S.; Ohno, T.; Fukuma, T. Direct Imaging of Atomic-Scale Surface Structures of Brookite TiO<sub>2</sub> Nanoparticles by Frequency Modulation Atomic Force Microscopy in Liquid. *J. Phys. Chem. C* **2018**, *122*, 24085–24093.

(38) Akrami, S. M. R.; Nakayachi, H.; Watanabe-Nakayama, T.; Asakawa, H.; Fukuma, T. Significant Improvements in Stability and Reproducibility of Atomic-Scale Atomic Force Microscopy in Liquid. *Nanotechnology* **2014**, *25*, 455701.

(39) Hutter, J.; Iannuzzi, M.; Schiffmann, F.; VandeVondele, J. CP2K: Atomistic Simulations of Condensed Matter Systems. *Wiley Interdiscip. Rev.: Comput. Mol. Sci.* **2014**, *4*, 15–25.

(40) Perdew, J. P.; Burke, K.; Ernzerhof, M. Generalized Gradient Approximation Made Simple. *Phys. Rev. Lett.* **1996**, *77*, 3865–3868.

(41) Grimme, S.; Antony, J.; Ehrlich, S.; Krieg, H. A Consistent and Accurate Ab Initio Parametrization of Density Functional Dispersion Correction (DFT-D) for the 94 Elements H–Pu. *J. Chem. Phys.* **2010**, *132*, 154104.

(42) Hartwigsen, C.; Goedecker, S.; Hutter, J. Relativistic Separable Dual-Space Gaussian Pseudopotentials from H to Rn. *Phys. Rev. B: Condens. Matter Mater. Phys.* **1998**, *58*, 3641–3662.

(43) VandeVondele, J.; Hutter, J. Gaussian Basis Sets for Accurate Calculations on Molecular Systems in Gas and Condensed Phases. *J. Chem. Phys.* **2007**, *127*, 114105.

(44) Zhang, C.; Donadio, D.; Gygi, F.; Galli, G. First Principles Simulations of the Infrared Spectrum of Liquid Water Using Hybrid Density Functionals. *J. Chem. Theory Comput.* **2011**, *7*, 1443–1449.

(45) Zhang, C.; Spanu, L.; Galli, G. Entropy of Liquid Water from Ab Initio Molecular Dynamics. *J. Phys. Chem. B* **2011**, *115*, 14190–14195.

(46) Schwegler, E.; Grossman, J. C.; Gygi, F.; Galli, G. Towards an Assessment of the Accuracy of Density Functional Theory for First Principles Simulations of Water. II. *J. Chem. Phys.* **2004**, *121*, 5400–5409.

(47) Jonsson, H.; Mills, G.; Jacobson, K. W. Nudged Elastic Band Method for Finding Minimum Energy Paths of Transitions. *Classical and Quantum Dynamics in Condensed Phase Simulations*, 1998; pp 385–404.

(48) Henkelman, G.; Uberuaga, B. P.; Jónsson, H. A Climbing Image Nudged Elastic Band Method for Finding Saddle Points and Minimum Energy Paths. *J. Chem. Phys.* **2000**, *113*, 9901.

(49) Arrhenius, S. Über die Dissociationswärme und den Einfluß der Temperatur auf den Dissociationsgrad der Elektrolyte. *Z. Phys. Chem.* **1889**, *4*, 96–116.

(50) Andrade, M. F. C.; Ko, H.-Y.; Zhang, L. F.; Car, R.; Selloni, A. Free Energy of Proton Transfer at the Water-TiO<sub>2</sub> Interface from Ab Initio Deep Potential Molecular. *Chem. Sci.* **2020**, *11*, 2335–2341.

(51) Takeuchi, M.; Sakamoto, K.; Martra, G.; Coluccia, S.; Anpo, M. Mechanism of Photoinduced Superhydrophilicity on the TiO<sub>2</sub> Photocatalyst Surface. *J. Phys. Chem. B* **2005**, *109*, 15422–15428.

(52) Miyauchi, M.; Nakajima, A.; Watanabe, T.; Hashimoto, K. Photocatalysis and Photoinduced Hydrophilicity of Various Metal Oxide Thin Films. *Chem. Mater.* **2002**, *14*, 2812–2816.

(53) Drelich, J.; Chibowski, E.; Meng, D. D.; Terpilowski, K. Hydrophilic and Superhydrophilic Surfaces and Materials. *Soft Matter* **2011**, *7*, 9804–9828.

(54) Zhang, L.; Dillert, R.; Bahnemann, D.; Vormoor, M. Photo-Induced Hydrophilicity and Self-Cleaning: Models and Reality. *Energy Environ. Sci.* **2012**, *5*, 7491–7507.

(55) Zubkov, T.; Stahl, D.; Thompson, T. L.; Panayotov, D.; Diwald, O.; Yates, J. T. Ultraviolet Light-Induced Hydrophilicity Effect on TiO<sub>2</sub>(110)(1×1): Dominant Role of the Photooxidation of Adsorbed Hydrocarbons Causing Wetting by Water Droplets. *J. Phys. Chem. B* **2005**, *109*, 15454–15462.

(56) Irie, H.; Hashimoto, K. Photocatalytic Active Surfaces and Photo-Induced High Hydrophilicity/High Hydrophobicity. In *Handbook of Environmental Chemistry Vol. 2 Environmental Photochemistry*; Robertson, P. K. J., Bahnemann, D. W., Boule, P., Eds.; Springer-Verlag: Heidelberg, Germany, 2005; pp 425–450.

(57) Litke, A.; Hensen, E. J. M.; Hofmann, J. P. Role of Dissociatively Adsorbed Water on the Formation of Shallow Trapped Electrons in TiO<sub>2</sub> Photocatalysts. *J. Phys. Chem. C* **2017**, *121*, 10153–10162.

(58) Fukuma, T.; Reischl, B.; Kobayashi, N.; Spijker, P.; Canova, F. F.; Miyazawa, K.; Foster, A. S. Mechanism of Atomic Force Microscopy Imaging of Three-Dimensional Hydration Structures at a Solid-Liquid Interface. *Phys. Rev. B: Condens. Matter Mater. Phys.* **2015**, *92*, 155412.

(59) Grotthuss, C. J. T. Sur la Décomposition de L'eau et des Corps Qu'elle Tient en Dissolution à L'aide de L'électricité Galvanique. *Ann. Chim.* **1806**, *58*, 54–74.

(60) Cukierman, S. Et tu Grotthuss! and Other Unfinished Stories. *Biochim. Biophys. Acta, Bioenerg.* **2006**, *1757*, 876–885.

(61) Hirshfeld, F. L. Bonded-Atom Fragments for Describing Molecular Charge Densities. *Theor. Chim. Acta* **1977**, *44*, 129–138.

(62) Young, D. C. *Computational Chemistry: A Practical Guide for Applying Techniques to Real World Problems*; Wiley: New York, 2001.

(63) Jiang, Q. G.; Ao, Z. M.; Li, S.; Wen, Z. Density Functional Theory Calculations on the CO Catalytic Oxidation on Al-Embedded Graphene. *RSC Adv.* **2014**, *4*, 20290–20296.

(64) Marx, D. Proton Transfer 200 Years after von Grotthuss: Insights from Ab Initio Simulations. *ChemPhysChem* **2006**, *7*, 1848–1870.

(65) Lentz, J.; Garofalini, S. H. Role of the Hydrogen Bond Lifetimes and Rotations at the Water/Amorphous Silica Interface on Proton Transport. *Phys. Chem. Chem. Phys.* **2019**, *21*, 12265–12278.